Fluctuation theorem convergence in a viscoelastic medium demonstrated experimentally using a dusty plasma

Dong Huang,[1] Shaoyu Lu,[1] Xia-qing Shi,[1] J. Goree,[2] and Yan Feng ●[1,*]

[1]*Center for Soft Condensed Matter Physics and Interdisciplinary Research,*
School of Physical Science and Technology, Soochow University, Suzhou 215006, China
[2]*Department of Physics and Astronomy, The University of Iowa, Iowa City, Iowa 52242, USA*

The convergence of the steady-state fluctuation theorem (SSFT) is investigated in a shear-flow experiment performed in a dusty plasma. This medium has a viscoelastic property characterized by the Maxwell relaxation time τ_M. Using measurements of the time series of the entropy production rate, for subsystems of various sizes, it is discovered that the SSFT convergence time decreases with the increasing system size until it eventually reaches a minimum value of τ_M, no matter the size of the subsystem. This result indicates that the convergence of the SSFT is limited by the energy-storage property of the viscoelastic medium.

I. INTRODUCTION

Unlike in the thermodynamic limit, the entropy production rate for a small system is a highly fluctuating quantity, which may even have negative transients. The probability of these events of negative entropy production are expressed by fluctuation theorems [1–9]. The steady-state fluctuation theorem (SSFT) is typically expressed as the convergence of the ratio between the probability of positive and negative entropy production rates, in the long-time limit,

$$\frac{1}{\tau} \ln \left[\frac{P(\sigma_\tau = +C)}{P(\sigma_\tau = -C)} \right] = C \text{ as } \tau \to \infty, \tag{1}$$

where σ_τ is the mean entropy-production rate over the time duration τ in the steady state, and $P(\sigma_\tau = C)$ is the probability that σ_τ equals the specified value of C.

This fluctuation theorem is useful for small systems, where the events with negative entropy production can be more easily detected. On the other hand, as the studied system size increases, the negative fluctuations become less frequent and the fluctuation theorem converges to the second law of thermodynamics [10].

Various experimental systems have been used for fluctuation experiments. These include colloids [11,12], quantum heat conduction [13], turbulence [10,14], and nonequilibrium bath systems [15]. In our literature search, we have found few previous studies of fluctuation theorems in viscoelastic materials, such as Ref. [16]; however, none of them investigated in particular the convergence time, as we do here.

The viscoelastic medium that we use is a strongly coupled dusty plasma, which is a four-component mixture of highly charged microspheres (dust), free electrons, ions, and neutral gas [17–33]. Due to their high charges and the related strong Coulomb interaction, these dust particles are strongly coupled [25]. When it flows, the collection of dust particles

exhibits viscoelasticity [34–38]. As demonstrated in [39], the viscoelastic property of dusty plasmas can be described reasonably well by the simple Maxwell model, characterized by the Maxwell relaxation time τ_M, as described in Appendix A. Like other strongly coupled systems, the viscoelasticity of dusty plasmas is the combination of the liquidlike viscous dissipation and the solidlike elasticity. For a shorter timescale $< \tau_M$, the solidlike energy-storing elasticity dominates [39]. For two-dimensional (2D) dusty plasmas [39], the value of τ_M is typically 3 to 5 times the inverse dusty plasma frequency ω_{pd}^{-1}.

Experiments with dusty plasmas have the advantage that they allow tracking the motion of individual particles, so that one can calculate the instantaneous shear stress $P_{xy}(t)$ and entropy production rate $\sigma(t)$, which are needed in the SSFT. This was exploited recently by Wong *et al.* [40], who analyzed small subsystems within a sheared flow in a liquidlike dusty plasma. In [40], it was confirmed that in a dusty plasma, there is a convergence time beyond which Eq. (1) is satisfied. However, the underlying physics that governs the value of this convergence time is still largely unknown. Moreover, the dependence of the convergence on the size of the subsystem also requires study. These are the questions that we investigate in this paper, using data from an experiment and supporting simulations.

The rest of this paper is organized as follows. In Sec. II, we introduce our dusty plasma experiment to investigate the SSFT, as well as the corresponding computer simulation methods. In Sec. III, we calculate the time series of the entropy production rate for various subsystems in our experiment. We find that the distribution of the averaged entropy production rate for various subsystems can be described as the Gaussian function. Then, based on the Gaussian distribution entropy production rate, the asymptotic trend of our experimental data to the SSFT is derived analytically. As a result, we obtain the dependence of the convergence time of the SSFT on the subsystem size, and find that the Maxwell relaxation time of viscoelasticity is the lower limit of the

———————
*fengyan@suda.edu.cn

convergence time. Our computer simulation results further confirm these findings. Finally, a summary of our findings is given in Sec. IV.

II. EXPERIMENT AND SIMULATION

The experiment for this SSFT study was performed in the setup similar to [28]. Using argon gas at 15.5 mTorr, capacitively coupled rf power was applied to generate a plasma. Introducing $\gtrsim 16\,000$ polymer microspheres of 8.1 μm diameter, they settled into a single horizontal layer, where they were levitated in a sheath above the lower electrode. A top-view video camera imaged ≈ 4400 dust particles in a field of view of (29.05×21.78) mm^2, at 55 frames per second. To generate a pair of counterpropagating dust flows, there were two oppositely directed laser beams, each with 0.95 W power. These were shaped into stripes of width 0.2 mm using scanning mirrors rastered in the x direction at 200 Hz, as in [28]. These manipulation laser beams drove a shear flow, leading to the shear-induced melting from the solid lattice, with a much more anisotropic feature in kinetic temperature than [40]. After the flow reached a steady state, a 12 s movie was recorded and analyzed to determine the coordinates and velocities of the dust particles in each frame. Note that in our dusty plasma experiment, the strength of the vertical confinement is generally two to three orders of magnitude larger than the in-plane confinement [41,42], so that as compared with the in-plane motion, the vertical displacement of dust particles can be ignored.

The parameters for the collection of dust particles were as follows. The spacing of particles was characterized by the Wigner-Seitz radius [22], $a = 0.21$ mm. As dust particles moved, they experienced gas damping at the rate [41] $\nu_f = 2.7$ s^{-1}. By analyzing wave spectra [43,44] for the thermal motion of the initial highly ordered lattice, before applying the manipulation lasers [28], we determined the charge on each dust particle, $Q = -8100e$, the screening parameter $\kappa = a/\lambda_D = 0.47$, and the nominal 2D dusty plasma frequency $\omega_{pd} = 86$ s^{-1}, which we will use to normalize the timescales.

The flow velocity of the dust particles was along the x axis, while the velocity had a gradient in the y direction, as shown by the time-averaged profile $\overline{V_x}$ in Fig. 1. To calculate $\overline{V_x}(y)$, we converted the velocity data for individual particles into data for a fluid flow by dividing the field of view into 103 bins (each with the width of a) and using the cloud-in-cell algorithm [30]. In the inset of Fig. 1, the two prominent peaks in the positive and negative directions correspond to two counterpropagating flows in the experiment, as in [28,45]. To illustrate the motion of dust particles in our experiment, we also present the superposition of particle positions for the time duration of 0.25 second in our analyzed movie, as shown in Fig. 2. Clearly, two counterpropagating dust flows can be observed in Fig. 2, where $y/a \approx 40$ and 60, respectively. In our data analysis, we mainly focus on the central region of the laminar flow, where the drift velocity is nearly linear, as the straight-line fit shown in Fig. 1, with a velocity gradient γ. To confirm the steady conditions in our experiment, we divide the movie into four portions to calculate the drift velocity profiles, so that the standard deviation of the velocity for each bin can be determined, as the error bar shown in Fig. 1.
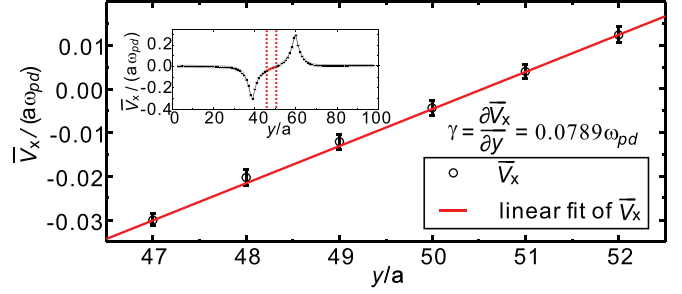

FIG. 1. Velocity profile in the dusty plasma experiment. Using laser manipulation, two counterpropagating dust flows were generated, as shown in the inset. The experiment was symmetric in the x direction, so that the flow velocity varied only with y. We mainly analyzed the central region, between the two dashed lines in the inset, where the velocity profile is nearly linear, as shown in the main panel. The slope of a linear fit yields the shear rate γ, which is used to calculate the entropy production rate. In the SSFT analysis, subsystems of different sizes were chosen; these spanned different ranges in the x direction, but always the same range of y from 47 a to 52 a.

To further verify our findings from the experiment, we also perform Langevin dynamical simulations to mimic our shear-induced melting dusty plasma experiment. In our simulations, we use the binary Yukawa repulsion with $N = 4096$ particles in a 2D plane, with the periodic boundary conditions. All simulation parameters are specified to be the same as our experiment conditions. For example, we choose the screening parameter as $\kappa = 0.47$, the initial coupling parameter as $\Gamma = 800$, and the frictional gas damping rate as $\nu_f = 0.031\,\omega_{pd}$. In fact, in addition to 4096 particles, we also perform a few test runs with 16 384 particles to make sure all of the presented results are not affected.

To mimic the strong dust particle flows generated by laser manipulation in our experiment, we introduce two external
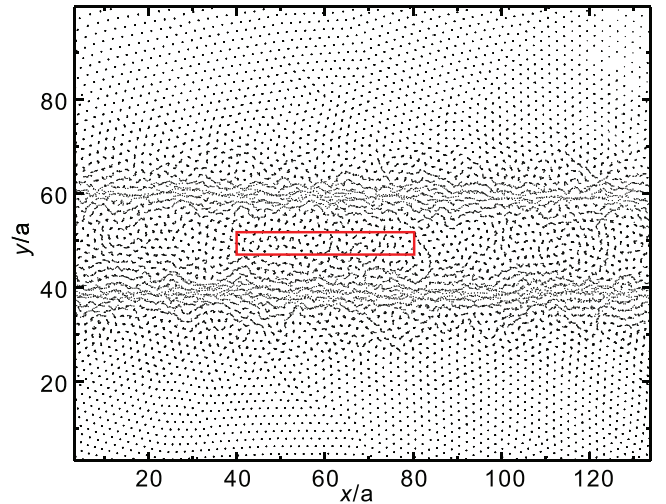

FIG. 2. Superposition of particle positions for the time duration of 0.25 second in our experiment. The rectangle around the central portion corresponds to the region of one typical subsystem with $N = 63$ dust particles in our reported data analysis.
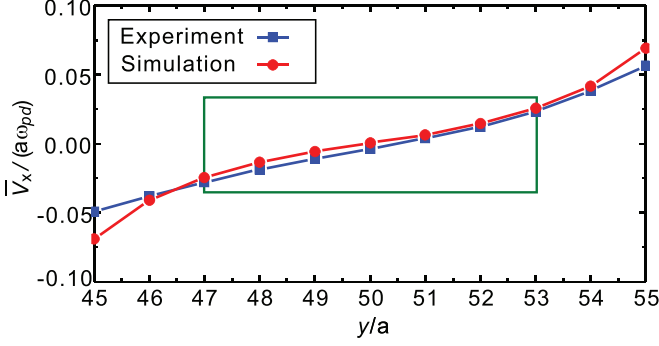
FIG. 3. Drift velocity profiles from our experiment and simulations. Using our specified force in our simulations, the resulting drift velocity in the central region is almost identical to our experiment results.

forces in two locations in our simulations. In our experiment, the strong dust particle flow was generated by scanning one powerful laser beam with the width of $\approx a$ in the x direction at 200 Hz, which is much higher than the nominal 2D dusty plasma frequency. Thus, in our simulations, the force to drive the particle flow is assumed to be localized in the y direction, with the width of $\approx a$, and also uniform in the x direction. To satisfy these requirements, we choose these two external forces as $\mathbf{F}_1 = A \exp[-(y - 11.08a)^2/0.25a^2]ma\omega_{pd}^2\mathbf{x}$ and $\mathbf{F}_2 = -A \exp[-(y + 11.08a)^2/0.25a^2]ma\omega_{pd}^2\mathbf{x}$ in the $\pm\mathbf{x}$ directions, respectively. The force amplitude A can be adjusted in simulations, so that one may calculate the resulting flow velocity profile to compare with the experimental result. For our simulation results reported here, we choose $A = 0.126$ because the resulting drift velocity in the central region is almost the same as that in our experiment, as shown in Fig. 3. Other simulation details are the same as [46].

III. RESULTS AND DISCUSSION

The time series $P_{xy}(t)$ of the shear stress was calculated [1,47,48] with an input of data for individual particle positions and velocities from our experiment. In the central melted region, the shear stress is calculated using

$$P_{xy} = \sum_{i=1}^{N}\left[m(v_{ix} - \overline{V_{x,i}})v_{iy} - \frac{1}{2}\sum_{j\neq i}^{N}\frac{x_{ij}y_{ij}}{r_{ij}}\frac{\partial\phi(r_{ij})}{\partial r_{ij}}\right], \quad (2)$$

where the drift motion $\overline{V_{x,i}}$ is removed, as in [40,46], and $\phi(r_{ij})$ is the binary interparticle Yukawa repulsion between the particles i and j, i.e., $\phi(r_{ij}) = Q^2 \exp(-r_{ij}/\lambda_D)/4\pi\epsilon_0 r_{ij}$. Here, we determine the drift velocity $\overline{V_{x,i}}$ for the particle i from the linear fit of the drift velocity $\overline{V_x}$ gradient of $\gamma = 0.0789\,\omega_{pd}$ in Fig. 1, and the corresponding y coordinate of the particle i. For the second term in Eq. (2) here, the interparticle force may include the pairs of the particles inside i and outside j of the studied subsystem. Thus, we choose a cutoff length of $r_{ij} \leqslant 10\,a$ for the particle pairs in our data analysis, to exclude the effects of all particles outside the field of view in our experiment, similar to [49].

Our obtained time series $P_{xy}(t)$ of the shear stress was used to obtain three quantities. First, it was used to

obtain the entropy production rate, $\sigma(t) = -P_{xy}(t)\gamma/k_BT$. Second, the Maxwell relaxation time τ_M was obtained from $C_s(t)$, the autocorrelation function of $P_{xy}(t)$. In particular, τ_M was identified as the time when $C_s(t)$ decays to $1/e$ of its initial value [48,50]. Third, we used $C_s(t)$ to obtain the the temperature T of the dust particles, without undue error arising from the finiteness of the subsystem and time duration, using [46] $k_BT = \gamma[\int_0^\infty C_s(t)dt]/\overline{P_{xy}}$.

For all three of these purposes, calculations were performed within subsystems of various small spatial sizes. Since the flow velocity varied with y, but not with x, we chose the subsystems to have various ranges of x but always the same range of y from $47\,a$ to $52\,a$. In our subsystems, the time-averaged numbers of dust particles are 6, 13, 19, 25, 32, 38, 44, 51, 57, and 63, respectively, and for each size of subsystem, we sample $\geqslant 4$ sets of data by varying the location of the x range, so that the uncertainties of these analyzed quantities can be determined, as the error bars shown in the latter figures. The rectangle drawn in Fig. 2 indicates the corresponding region of one typical subsystem with $N = 63$ dust particles in our data analysis. In fact, the number of dust particles inside this fixed-region subsystem fluctuates around 63 briefly, with the 48% observation time of 63 particles or the 86% observation time of 61 to 65 particles, mainly due to the density fluctuation and the nonuniformity of the shear-induced melting.

As an example, the time series of our calculated entropy production rate per unit area $\sigma(t)/A$ is presented in Fig. 4(a), for the subsystem with $N = 32$ particles. Clearly, the obtained $\sigma(t)$ fluctuates around a positive average value, as expected for the second law of thermodynamics, but sometimes it fluctuates negatively as one would expect for the SSFT.

Besides the time series of $\sigma(t)$, the averaged entropy production rate within the time duration τ, $\sigma_\tau = [\int_0^\tau \sigma(t)dt]/\tau$, is calculated to characterize its behaviors within different time intervals. In Fig. 4(b), we present distributions of σ_τ for different time intervals, all for a fixed subsystem size of $N = 32$. Similarly, for a fixed time interval of $\tau\omega_{pd} = 1.57$, we also prepared distributions of σ_τ for various sizes of subsystems in Fig. 4(c). We find that these distributions of σ_τ/A are well fit by a Gaussian distribution,

$$P(\sigma_\tau) = \exp\left[-(\sigma_\tau - \bar{\sigma})^2\big/\left(2\sigma_{d,\tau}^2\right)\right]/(\sqrt{2\pi}\sigma_{d,\tau}), \quad (3)$$

as the curves show in Figs. 4(b) and 4(c). In Eq. (3), $\sigma_{d,\tau}^2$ is the variance of σ_τ, and $\bar{\sigma}$ is the average of σ_τ. Clearly, as the time duration increases, in Fig. 4(b), or as the subsystem size increases, in Fig. 4(c), $\sigma_{d,\tau}^2$ becomes smaller, i.e., the Gaussian distribution becomes narrower, while $\bar{\sigma}$ is almost unchanged.

The results in Figs. 4(b) and 4(c) show that the extension of the time duration and the expansion of the system size both suppress the σ_τ fluctuations, and the distribution of σ_τ becomes narrower. As a result, the probability of the negative σ_τ/A events is reduced, indicating that the second law of thermodynamics is obeyed more. The fitting result of $\bar{\sigma}$ just corresponds to the viscous heating term $-\eta\gamma^2/k_BT$ [28,48,51], where η is the viscosity, so that for the same subsystem of $N = 32$, the peak location of the Gaussian fitting is unchanged in Fig. 4(b). In Fig. 4(c), the peak location from fitting varies briefly, probably due to the nonuniformity in the
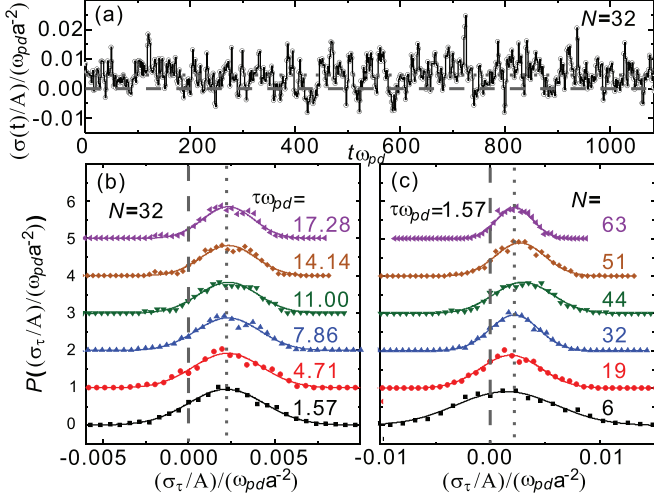
FIG. 4. (a) Time series of the entropy production rate per unit area $\sigma(t)/A$ for the subsystem of $N = 32$ dust particles and (b) the corresponding distribution of the entropy production rate σ_τ/A averaged for different time durations, as well as (c) the distribution of σ_τ/A of different subsystems for the same time duration of $t\omega_{pd} = 1.57$. For all panels, the dotted and dashed lines correspond to the averaged and zero entropy production rates, respectively. In (b) and (c), we find that our obtained distributions of σ_τ/A can fit to a Gaussian distribution quite well. When the time duration increases in (b) or the subsystem size increases in (c), the negative entropy production rate always occurs less frequently. In (b) and (c), the center of the Gaussian fit is almost unchanged, suggesting that the averaged entropy production rate is an unchanged positive value due to viscous heating. Note that for clarity, we lift different distributions upward in steps of unity and magnify the vertical probability 10 times in (b) and (c).

x direction in our experiment, and the viscous heating effect fluctuates for various sizes of subsystems.

According to the SSFT, as the time duration increases, the left-hand side (LHS) of Eq. (1) gradually approaches the RHS of Eq. (1), C. For convenience, we define the left side of Eq. (1) as $f(\sigma_\tau)$, i.e., $f(\sigma_\tau) = \{\ln[P(\sigma_\tau)/P(-\sigma_\tau)]\}/\tau$, so that the SSFT is just $\lim_{\tau \to \infty} f(\sigma_\tau) = \sigma_\tau$.

As shown in Fig. 5(a), the results of $f(\sigma_\tau)$ for different time durations are plotted as a function of σ_τ, calculated from Fig. 4(a). For each time duration, the $f(\sigma_\tau)$ results show the linear relationship with σ_τ, as the linear fit shown with the straight lines. This linear characteristic of $f(\sigma_\tau)$ is the key evidence of the SSFT [7]. More importantly, as the time duration increases, the linear fit gradually converges to the dashed line of the RHS of Eq. (1), indicating that Eq. (1) of the SSFT is then satisfied.

To quantify this asymptotic behavior of the linear fit in Fig. 5(a), we define this discrepancy D as

$$D = \text{slope} (f(\sigma_\tau)) - \text{slope}(\sigma_\tau) \tag{4}$$

$$= \left(2\frac{\bar{\sigma}}{\sigma_{d,\tau}^2 \tau} \right) - 1, \tag{5}$$

which is the discrepancy of the slopes between the solid and dashed lines in Fig. 5(a), for various time durations. Here, Eq. (5) is our simplified version of Eq. (4) derived from the
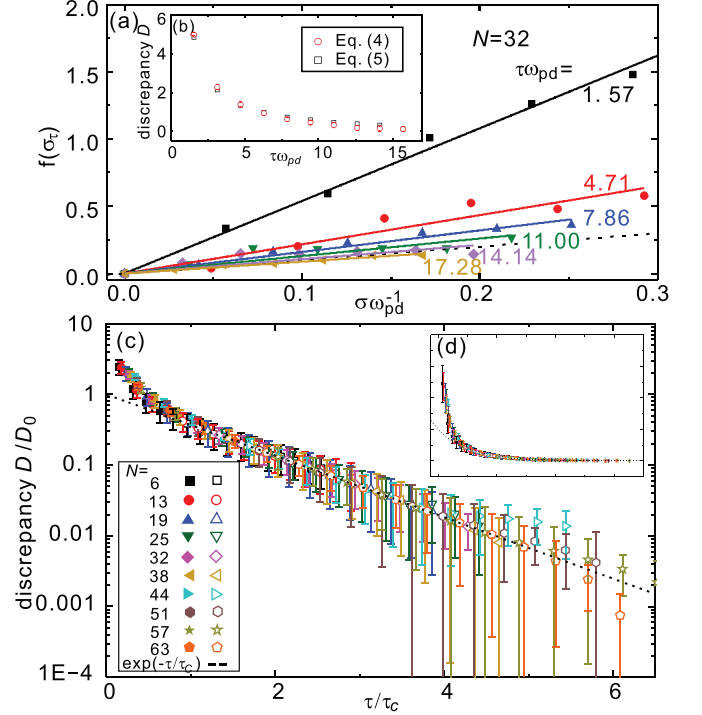

FIG. 5. Obtaining the SSFT convergence time τ_C. (a) Variation trends of the LHS of Eq. (1) for different τ values; (b) discrepancies between the two sides of Eq. (1). In (a), the symbols are $\frac{1}{\tau} \ln[\frac{P(\sigma_\tau = +C)}{P(\sigma_\tau = -C)}]$, the LHS of Eq. (1), calculated from Fig. 4(a), exhibiting the linear feature. Solid lines in (a) are the linear fit of the symbols, while the dashed line corresponds to the RHS of Eq. (1). As the time duration increases, clearly the linear fit converges to the dashed line, following the SSFT. In (b), we use Eq. (4) to quantify the discrepancy D of the slopes between the solid and dashed lines in (a), for various time durations. For the Gaussian distribution of σ_τ, as for our system in Fig. 4, Eq. (4) can be simplified to Eq. (5), as verified from the data points overlapping in (b). In (c) and (d), with logarithmic and linear coordinates, respectively, we use the values from Eq. (5) to represent the discrepancy D of the two sides of Eq. (1) for various subsystem sizes. From Appendix C, the decay of Eq. (5) for the Gaussian distribution of σ_τ contains two timescales, and we mainly focus on the longer one, so that we ignore the first four data points for each set, marked as filled symbols. We find that all open symbols in (c), i.e., the discrepancy for longer times, can fit $D_0 \exp(-\tau/\tau_C)$ well. The result of this analysis is the fit parameter τ_C, for the convergence time of the SSFT.

combination of Eqs. (1) and (3), described in Appendix B, valid for any systems with the Gaussian distribution entropy production rates. The calculated results of D from the data in Fig. 5(a) are presented in Fig. 5(b), with two sets of data corresponding to Eqs. (4) and (5), respectively. Clearly, as the time duration increases, the discrepancy D diminishes monotonically to zero, as predicted by the SSFT. These two sets of data in Fig. 5(b) are almost the same, further suggesting that our simplified Eq. (5) from the Gaussian distribution can be used with our experimental data analysis, as we will use later. Besides the discrepancy D data for the subsystem of $N = 32$ in Fig. 5(b), we also calculate the discrepancy of various time durations for all other studied subsystems, as in Fig. 5(c).
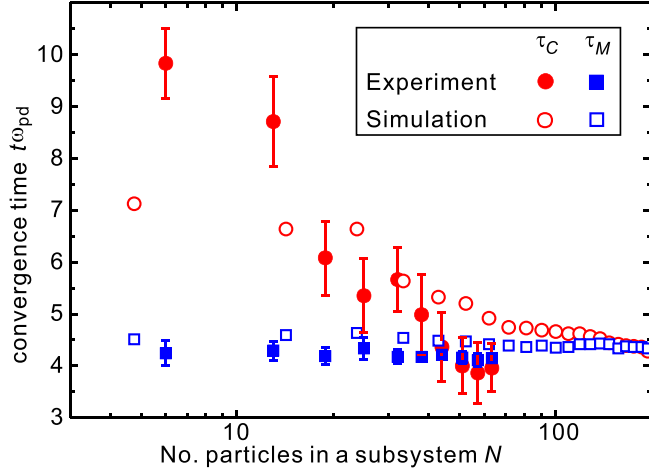
FIG. 6. Convergence times of SSFT τ_C for various subsystems, compared to the Maxwell relaxation times τ_M. We discover that as the analyzed system size increases, the convergence time of SSFT τ_C rapidly decreases, but this decrease ceases when τ_C reaches a minimum value that nearly matches the Maxwell relaxation time τ_M. This is our chief result, which we attribute to the elastic property that dominates our viscoelastic substance at short timescales.

After our further derivation in Appendix C, we find that the key term in Eq. (5) can be expressed as

$$\sigma_{d,\tau}^2 \tau = I_1 - I_2. \tag{6}$$

Here, I_1 and I_2 are two time integrals, suggesting that $\sigma_{d,\tau}\tau$ exhibits the long-time and short-time convergence behaviors, respectively. The convergence of Eq. (5) is mainly dominated by the behavior of the long-time integral of I_1 from Appendix C, so that we mainly focus on the determination of the convergence timescale of I_1 from our calculated D. Since the timescale of I_1 is much longer than that of I_2, the obtained discrepancy D data at longer times are almost completely from I_1, such as those in Fig. 5(b). Thus, for each subsystem, we always ignore the first four data points of D, marked as the filled symbols in Fig. 5(c), and only focus on the later data points, marked as the open symbols.

We obtain the convergence time τ_C using these discrepancy data. For each subsystem, we fit the obtained discrepancy D to an exponential, starting from the fifth data point using the expression of $D_0 \exp(-\tau/\tau_C)$. This fit, as the dashed line shown in Fig. 5(c), has two free parameters: D_0 and τ_C. This fit is good, indicating that the long-time convergence trend of the discrepancy is exponential, no matter whether the system size varies, consistent with [40]. The result of this fitting that is of greatest interest to us is the convergence time, τ_C. The discrepancy D data and the fitting result from Fig. 5(c) are also replotted in Fig. 5(d) in linear coordinates, to show their asymptotic feature.

The Maxwell relaxation time was also determined for various subsystem sizes. The Maxwell relaxation time τ_M, shown as square symbols in Fig. 6, was obtained as the $1/e$ decay time of $C_s(t)$, the autocorrelation function of the fluctuations of the shear stress P_{xy} [48,50], as described in detail in Appendix A. Generally, the Maxwell relaxation time here is in the range of $4 < \tau_M \omega_{pd} < 4.5$.

As the major result of this paper, we find that the SSFT convergence time τ_C decreases with the increasing system size only until it reaches a minimum value, which is the Maxwell relaxation time τ_M. This result is clearly presented in Fig. 6, where the filled circular symbols of the convergence times τ_C are obtained from fitting in Fig. 5(c). Clearly, as the subsystem size increases, this convergence time τ_C decreases rapidly at first, but this decrease ceases at a minimum convergence time and thereafter becomes a constant. That minimum convergence time is $\tau_C \omega_{pd} \approx 4$, which nearly matches the Maxwell relaxation time.

We provide our interpretation of the convergence time of SSFT in our experiment, which has its minimum of the Maxwell relaxation time. This result can be regarded as a consequence of the elastic properties of a viscoelastic substance. It seems that the SSFT convergence time τ_C is always limited, which means that Eq. (1) is not satisfied when the timescale is shorter than this limit, no matter how large the studied system. For the sheared flow systems where the entropy production rate mainly arises from viscous heating, as studied here, this limit of τ_C equals the Maxwell relaxation time τ_M. For a viscoelastic substance, the energy-storing elastic effects dominate for the timescales shorter than τ_M, while at the longer timescales, the dissipative viscous property is dominant. The entropy production rate studied here arises only from the dissipative processes.

To further verify the experimental result that the convergence time trends toward a minimum value of the Maxwell relaxation time, we also perform the same calculations using our Langevin simulation data. The advantage of our simulation is that the much longer time duration provides much better statistics than in the experiment, and also allows us to vary the subsystem size over a wider range. The calculation procedure of the time series of the shear stress and the latter physical quantities in our simulations is exactly the same as our experiment data analysis. We also confirm that the distribution of the entropy production rate per unit area σ_τ/A can also be described as the Gaussian, the same as the experiment result. From Fig. 6, clearly, the obtained results of τ_C and τ_M from our simulation follow the same variation trend as those from our experiment. Especially for the larger system size, τ_C diminishes to a minimum value of $\approx 4\omega_{pd}^{-1}$ which nearly matches the Maxwell relaxation time τ_M, as in the experiment. In short, all of our experimental findings described above are further verified from our simulations.

IV. SUMMARY

In summary, we studied the SSFT using the entropy production rate in our sheared flow dusty plasma experiment with various subsystem sizes containing 6 to 63 dust particles. Using the observed particle positions and velocities in our experiment, we calculate the time series of the entropy production rate for various subsystems. For various subsystems, it is found that the distribution of the averaged entropy production rate can be fit to the Gaussian function quite well. Using the Gaussian distribution entropy production rate, we derive the analytical expression of the asymptotic trend of our experimental data to the SSFT, given by Eqs. (4) and (5). Based on these obtained data, we find that as the

subsystem size gradually increases, the SSFT convergence times τ_C gradually diminish until reaching the minimum, which is just the Maxwell relaxation time τ_M. Using our Langevin simulations, these findings are further verified by a wider range of the subsystem size. We interpret the observed minimum convergence time as a consequence of the elastic properties of a viscoelastic substance. For other experiments, such as the heat conduction or convection dominated systems, the corresponding SSFT convergence time may be quite different from our current result, which can be studied in the future.

APPENDIX A: THE MAXWELL MODEL

It is widely known that most materials in nature are viscoelastic [28,52], which means that they exhibit both the liquidlike viscous and the solidlike elastic properties to the mechanical disturbance. In the viscoelasticity theory, to characterize the viscoelastic property, the frequency-dependent viscosity $\eta(\omega)$ [30], i.e., the viscous and elastic properties varying with the frequency (or different timescales), is obtained using the Laplace-Fourier transformation of

$$\eta(\omega) = \frac{1}{A k_B T} \int_0^\infty \langle P_{xy}(t) P_{xy}(0) \rangle e^{i\omega t} dt. \quad (A1)$$

Here, P_{xy} is the off-diagonal element of the stress tensor, $k_B T$ is the kinetic temperature, and A is the area of the analyzed region for 2D systems. In general, $\eta(\omega)$ is a complex function, which is

$$\eta(\omega) = \eta'(\omega) - i\eta''(\omega), \quad (A2)$$

with the real part $\eta'(\omega)$ corresponding to the viscous property, and the imaginary part $\eta''(\omega)$ corresponding to the elastic property. Based on the viscoelastic approximation [48], $\eta(\omega)$ can be expressed as

$$\eta(\omega) = \frac{G_\infty}{-i\omega + 1/\tau_M}, \quad (A3)$$

where G_∞ is an instantaneous (high-frequency) modulus of rigidity, and the τ_M is the Maxwell relaxation time. As a result, for the shorter timescales of $\omega^{-1} \ll \tau_M$, the response of the material is dominated by the solidlike elastic property, corresponding to the energy storage, while for the longer timescales of $\omega^{-1} \gg \tau_M$, the response of the material is dominated by the liquidlike viscous property, corresponding to the energy dissipation. The real and imaginary parts of Eq. (A3) can also be expressed as [28]

$$\eta'(\omega)/\eta_0 = \frac{1}{1 + \tau_M^2 \omega^2} \quad (A4)$$

and

$$\eta''(\omega)/\eta_0 = \frac{\tau_M \omega}{1 + \tau_M^2 \omega^2}. \quad (A5)$$

The Maxwell relaxation time refers to the timescale when the real and imaginary parts of the frequency dependence $\eta(\omega)$ are the same, i.e., $\omega = 1/\tau_M$, as in [39]. Typically, to determine the Maxwell relaxation time τ_M, one can calculate the autocorrelation function of stress fluctuation, $\langle P_{xy}(t) P_{xy}(0) \rangle$, and then determine the time when this autocorrelation function falls to $1/e$ of its initial value [48,50], as we do in the main text.

APPENDIX B: DERIVATION OF EQ. (5)

Here, we present our detailed derivation of the discrepancy D expression of Eq. (5), from the combination of Eq. (4) and the Gaussian distribution of σ_τ. From Fig. 4, we find that the distribution of the entropy production rate σ_τ in our experiment can be described as the Gaussian distribution, given by Eq. (3), quite well. In Eq. (3), $\bar\sigma$ is the average of the time series of $\sigma(t)$ over the whole time duration, and $\sigma_{d,\tau}^2$ is the variance for σ_τ. Thus, from the Gaussian distribution function, we obtain

$$\frac{P(\sigma_\tau)}{P(-\sigma_\tau)} = \exp\left(2 \frac{\sigma_\tau \bar\sigma}{\sigma_{d,\tau}^2} \right). \quad (B1)$$

On the other hand, the steady-state fluctuation theorem (SSFT) predicts the ratio of the relative probabilities as

$$\frac{1}{\tau} \ln\left[\frac{P(\sigma_\tau)}{P(-\sigma_\tau)} \right] = \sigma_\tau \text{ as } \tau \to \infty, \quad (B2)$$

which is just Eq. (1). After comparing Eq. (B1) with Eq. (B2), we obtain

$$\frac{1}{\tau} \ln\left[\frac{P(\sigma_\tau)}{P(-\sigma_\tau)} \right] = 2 \frac{\bar\sigma}{\sigma_{d,\tau}^2 \tau} \sigma_\tau, \quad (B3)$$

which is the SSFT form for the Gaussian distribution of σ_τ.

For convenience, we define the LHS of Eq. (B3) as $f(\sigma_\tau)$, so that the SSFT is expressed as $\lim_{\tau \to \infty} f(\sigma_\tau) = \sigma_\tau$. As a result, the discrepancy D can be simplified as

$$D = \text{slope}(f(\sigma_\tau)) - \text{slope}(\sigma_\tau) = \left(2 \frac{\bar\sigma}{\sigma_{d,\tau}^2 \tau} \right) - 1, \quad (B4)$$

which is just Eq. (5). This expression indicates that for the Gaussian distribution of σ_τ, this discrepancy D can be analytically expressed as the function of the time duration τ, as well as the variance and the mean value of σ_τ.

APPENDIX C: DERIVATION OF EQ. (6)

Here, we present our detailed derivation of Eq. (6). In Eq. (5), or Eq. (4), the mean value of σ_τ for our observed dust flow is a constant value, corresponding to the dotted line in Fig. 4(a). As a result, the variation of D purely depends on the change of $\sigma_{d,\tau}^2 \tau$ as the time goes. We know that the variance of σ_τ is defined as

$$\sigma_{d,\tau}^2 = \langle (\sigma_\tau - \bar\sigma)^2 \rangle$$

$$= \left\langle \frac{1}{\tau^2} \left\{ \int_0^\tau [\sigma(s_1) - \bar\sigma] ds_1 \right\} \left\{ \int_0^\tau [\sigma(s_2) - \bar\sigma] ds_2 \right\} \right\rangle$$
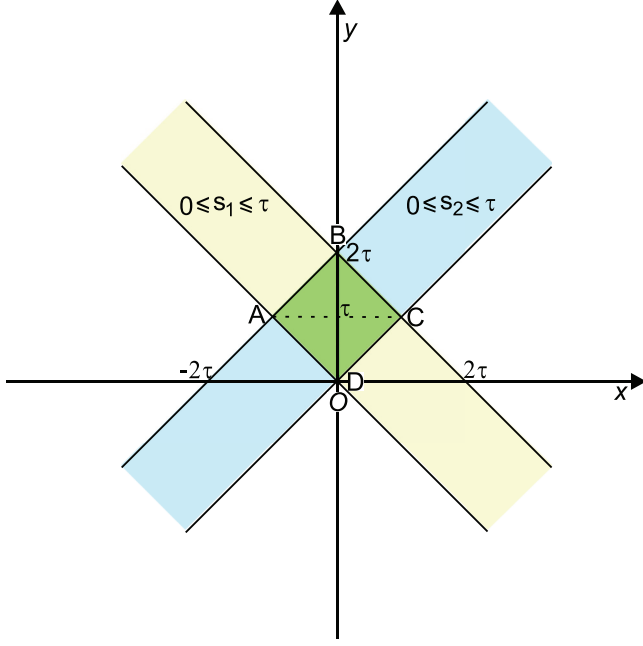
FIG. 7. Sketch of the integral region in the x-y coordinate system for Eq. (C2). Using changing variables of $x = s_1 - s_2$, $y = s_1 + s_2$ in Eq. (C2), the integral region of $0 \leqslant s_1 \leqslant \tau$ and $0 \leqslant s_2 \leqslant \tau$ in the s_1-s_2 coordinate is changed to $0 \leqslant x + y \leqslant 2\tau$ and $0 \leqslant y - x \leqslant 2\tau$ in the x-y coordinate, as the square with the four corners of $ABCD$ shown here. To simplify the later derivation, we divide this square into two triangles of $\triangle ABC$ and $\triangle ADC$ next.

$$= \frac{1}{\tau^2} \int_0^\tau ds_1 \int_0^\tau \langle [\sigma(s_1) - \bar\sigma][\sigma(s_2) - \bar\sigma]\rangle ds_2$$

$$= \frac{1}{\tau^2} \iint_S \langle [\sigma(s_1) - \bar\sigma][\sigma(s_2) - \bar\sigma]\rangle ds_1 ds_2. \quad (C1)$$

Here, the integral region S is in the squared region of $0 \leqslant s_1 \leqslant \tau$ and $0 \leqslant s_2 \leqslant \tau$. For convenience, we define $J(t) = \sigma(t) - \bar\sigma$ as the fluctuation of σ. Then, we change the variables as $x = s_1 - s_2$ and $y = s_1 + s_2$, following the integral transformation rule [53]. Thus, Eq. (C1) above can be rewritten as

$$\sigma_{d,\tau}^2 = \frac{1}{\tau^2} \iint_S \langle [J(s_1)][J(s_2)]\rangle ds_1 ds_2$$

$$= \frac{1}{\tau^2} \iint_{SD} \left\langle \left[J\left(\frac{x+y}{2}\right)\right]\left[J\left(\frac{y-x}{2}\right)\right]\right\rangle \left|\frac{\partial(s_1,s_2)}{\partial(x,y)}\right| dxdy, \quad (C2)$$

where $|\frac{\partial(s_1,s_2)}{\partial(x,y)}|$ is the Jacobi determinant. In our integral transformation, $|\frac{\partial(s_1,s_2)}{\partial(x,y)}| = |\begin{smallmatrix} 0.5 & 0.5 \\ -0.5 & 0.5 \end{smallmatrix}| = 0.5$ with the integral region, which satisfies the two conditions of $0 \leqslant x + y \leqslant 2\tau$ and $0 \leqslant y - x \leqslant 2\tau$ simultaneously, as the square with the four corners of $ABCD$ shown in Fig. 7. To simplify the derivation later, we divide this square of $ABCD$ into two triangles of $\triangle ADC$ and $\triangle ABC$, as shown in Fig. 7, so

that

$$\sigma_{d,\tau}^2 = \frac{1}{2\tau^2} \iint_{\triangle ADC} \left\langle \left[J\left(\frac{x+y}{2}\right)\right]\left[J\left(\frac{y-x}{2}\right)\right]\right\rangle dxdy$$

$$+ \frac{1}{2\tau^2} \iint_{\triangle ABC} \left\langle \left[J\left(\frac{x+y}{2}\right)\right]\left[J\left(\frac{y-x}{2}\right)\right]\right\rangle dxdy. \quad (C3)$$

For the integral region of $\triangle ADC$, we can convert the integral to

$$\iint_{\triangle ADC} \left\langle \left[J\left(\frac{x+y}{2}\right)\right]\left[J\left(\frac{y-x}{2}\right)\right]\right\rangle dxdy$$

$$= \int_0^\tau dy \int_{-y}^y \left\langle \left[J\left(\frac{x+y}{2}\right)\right]\left[J\left(\frac{y-x}{2}\right)\right]\right\rangle dx. \quad (C4)$$

For the integral region of $\triangle ABC$, we can convert the integral to

$$\iint_{\triangle ABC} \left\langle \left[J\left(\frac{x+y}{2}\right)\right]\left[J\left(\frac{y-x}{2}\right)\right]\right\rangle dxdy$$

$$= \int_\tau^{2\tau} dy \int_{y-2\tau}^{2\tau-y} \left\langle \left[J\left(\frac{x+y}{2}\right)\right]\left[J\left(\frac{y-x}{2}\right)\right]\right\rangle dx$$

$$= \int_\tau^0 d(-z) \int_{-z}^z \left\langle \left[J\left(\frac{x+2\tau-z}{2}\right)\right]\left[J\left(\frac{2\tau-z-x}{2}\right)\right]\right\rangle dx$$

$$= \int_0^\tau dz \int_{-z}^z \left\langle \left[J\left(\frac{x+2\tau-z}{2}\right)\right]\left[J\left(\frac{2\tau-z-x}{2}\right)\right]\right\rangle dx$$

$$= \int_0^\tau dz \int_{-z}^z \left\langle \left[J\left(\frac{x-z}{2}\right)\right]\left[J\left(\frac{-z-x}{2}\right)\right]\right\rangle dx$$

$$= \int_0^\tau dz \int_{-z}^z \left\langle \left[J\left(\frac{x+z}{2}\right)\right]\left[J\left(\frac{z-x}{2}\right)\right]\right\rangle dx. \quad (C5)$$
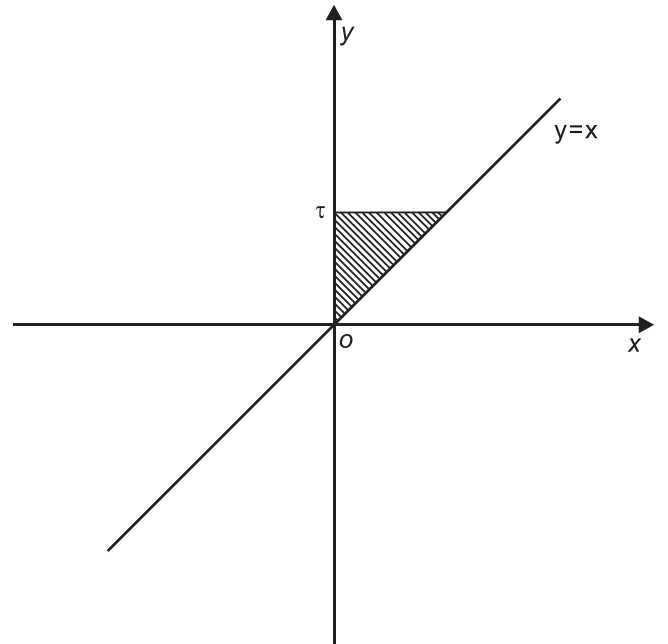

FIG. 8. Sketch of the integral region for Eq. (C6), the shaded region in the x-y coordinate system. In Eq. (C6), we swap the integral order of variables, so that the integral is simplified as $I_1 + I_2$.

Here, we use the variable z to replace the variable y as $z = 2\tau - y$. We also simplify the expressions of $\langle[J(\frac{x+2\tau-z}{2})][J(\frac{2\tau-z-x}{2})]\rangle = \langle[J(\frac{x-z}{2})][J(\frac{-z-x}{2})]\rangle$ and $\langle[J(\frac{x-z}{2})][J(\frac{-z-x}{2})]\rangle = \langle[J(\frac{x+z}{2})][J(\frac{z-x}{2})]\rangle$, using the translation invariance of the correlation function [54], because only the difference between the two variables of the correlation function (which are both x here) determines the final integral. Thus, the integral of Eq. (C5) is just the same as Eq. (C4). As a result, we get

$$\sigma_{d,\tau}^2 = \frac{1}{\tau^2} \int_0^\tau dy \int_{-y}^y \left\langle \left[J\left(\frac{x+y}{2}\right)\right]\left[J\left(\frac{y-x}{2}\right)\right]\right\rangle dx$$

$$= \frac{2}{\tau^2} \int_0^\tau dy \int_0^y \langle[J(x)][J(0)]\rangle dx, \qquad (C6)$$

also from the translation invariance of the correlation function [54] in the last step. Finally, we swap the integral order of variables of Eq. (C6) from Fig. 8 to get

$$\tau\sigma_{d,\tau}^2 = \frac{2}{\tau} \int_0^\tau dy \int_0^y \langle[J(x)][J(0)]\rangle dx$$

$$= \frac{2}{\tau} \int_0^\tau dx \int_x^\tau \langle[J(x)][J(0)]\rangle dy$$

$$= \frac{2}{\tau} \int_0^\tau \langle[J(x)][J(0)]\rangle(\tau - x)dx$$

$$= 2 \int_0^\tau \langle[J(x)][J(0)]\rangle dx$$

$$- \frac{2}{\tau} \int_0^\tau \langle[J(x)][J(0)]\rangle x dx$$

$$= I_1 - I_2, \qquad (C7)$$

where

$$I_1 = 2 \int_0^\tau \langle[J(x)][J(0)]\rangle dx \qquad (C8)$$

and

$$I_2 = \frac{2}{\tau} \int_0^\tau \langle[J(x)][J(0)]\rangle x dx. \qquad (C9)$$

We know that as τ increases, $\langle[J(x)][J(0)]\rangle$ in Eq. (C8) is an autocorrelation function of $J(x)$, indicating that I_1 increases gradually and approaches to a constant value of the total integral of this autocorrelation function when τ increases to infinity. However, since there is a denominator of τ in Eq. (C9), as τ increases, I_2 decays quickly to 0. From Eq. (C7), the value of $\tau\sigma_{d,\tau}^2$ is mainly determined by the value of I_1 as τ increases. Thus, when the value of τ is larger, as the time range for our data fitting in Fig. 5(c) increases, the value of $\tau\sigma_{d,\tau}^2$ is almost completely determined by I_1.

[1] D. J. Evans and G. P. Morriss, *Statistical Mechanics of Nonequilibrium Liquids* (Academic, London, 1990).

[2] D. J. Evans, E. G. D. Cohen, and G. P. Morriss, Phys. Rev. Lett. **71**, 2401 (1993).

[3] D. J. Evans and D. J. Searles, Adv. Phys. **51**, 1529 (2002).

[4] U. Seifert, Eur. Phys. J. B **64**, 423 (2008).

[5] H. K. Lee, C. Kwon, and H. Park, Phys. Rev. Lett. **110**, 050602 (2013).

[6] U. Seifert, Phys. Rev. Lett. **95**, 040602 (2005).

[7] G. Gallavotti and E. G. D. Cohen, Phys. Rev. Lett. **74**, 2694 (1995).

[8] G. E. Crooks, Phys. Rev. E **60**, 2721 (1999).

[9] K. Feitosa and N. Menon, Phys. Rev. Lett. **92**, 164301 (2004).

[10] D. Nickelsen and A. Engel, Phys. Rev. Lett. **110**, 214501 (2013).

[11] G. M. Wang, E. M. Sevick, E. Mittag, D. J. Searles, and D. J. Evans, Phys. Rev. Lett. **89**, 050601 (2002).

[12] J. Mehl, B. Lander, C. Bechinger, V. Blickle, and U. Seifert, Phys. Rev. Lett. **108**, 220601 (2012).

[13] K. Saito and A. Dhar, Phys. Rev. Lett. **99**, 180601 (2007).

[14] E. Falcon, S. Aumâitre, C. Falćon, C. Laroche, and S. Fauve, Phys. Rev. Lett. **100**, 064503 (2008).

[15] J. R. Gomez-Solano, A. Petrosyan, and S. Ciliberto, Phys. Rev. Lett. **106**, 200602 (2011).

[16] D. M. Heyes, D. Dini, and E. R. Smith, J. Chem. Phys. **148**, 194506 (2018).

[17] H. M. Thomas and G. E. Morfill, Nature (London) **379**, 806 (1996).

[18] L. I, W. Juan, C. Chiang, and J. Chu, Science **272**, 1626 (1996).

[19] A. Melzer, A. Homann, and A. Piel, Phys. Rev. E **53**, 2757 (1996).

[20] U. Konopka, G. E. Morfill, and L. Ratke, Phys. Rev. Lett. **84**, 891 (2000).

[21] R. L. Merlino and J. A. Goree, Phys. Today **27**, 32 (2004).

[22] G. J. Kalman, P. Hartmann, Z. Donkó, and M. Rosenberg, Phys. Rev. Lett. **92**, 065001 (2004).

[23] V. E. Fortov, A. V. Ivlev, S. A. Khrapak, A. G. Khrapak, and G. E. Morfill, Phys. Rep. **421**, 1 (2005).

[24] V. Nosenko, S. Zhdanov, A. V. Ivlev, G. Morfill, J. Goree, and A. Piel, Phys. Rev. Lett. **100**, 025003 (2008).

[25] G. E. Morfill and A. V. Ivlev, Rev. Mod. Phys. **81**, 1353 (2009).

[26] M. Bonitz, C. Henning, and D. Block, Rep. Prog. Phys. **73**, 066501 (2010).

[27] A. Piel, *Plasma Physics* (Springer, Heidelberg, 2010).

[28] Y. Feng, J. Goree, and B. Liu, Phys. Rev. Lett. **104**, 165003 (2010).

[29] P. Hartmann, A. Douglass, J. C. Reyes, L. S. Matthews, T. W. Hyde, A. Kovács, and Z. Donkó, Phys. Rev. Lett. **105**, 115004 (2010).

[30] Y. Feng, J. Goree, and B. Liu, Phys. Rev. Lett. **109**, 185002 (2012).

[31] A. Schella, M. Mulsow, A. Melzer, J. Schablinski, and D. Block, Phys. Rev. E **87**, 063102 (2013).

[32] E. Thomas, Jr., B. Lynch, U. Konopka, R. L. Merlino, and M. Rosenberg, Phys. Plasmas **22**, 030701 (2015).

[33] F. Wieben and D. Block, Phys. Rev. Lett. **123**, 225001 (2019).

[34] C. L. Chan and L. I, Phys. Rev. Lett. **98**, 105002 (2007).

[35] Z. Donkó, J. Goree, and P. Hartmann, Phys. Rev. E **81**, 056404 (2010).

[36] Y. Feng, J. Goree, and B. Liu, Phys. Rev. Lett. **105**, 025002 (2010).

[37] J. P. Mithen, Phys. Rev. E **89**, 013101 (2014).

[38] V. S. Dharodi, S. K. Tiwari, and A. Das, Phys. Plasmas **21**, 073705 (2014).

[39] Y. Feng, J. Goree, and B. Liu, Phys. Rev. E **85**, 066402 (2012).

[40] C. S. Wong, J. Goree, Z. Haralson, and B. Liu, Nat. Phys. **14**, 21 (2018).

[41] B. Liu, K. Avinash, and J. Goree, Phys. Rev. Lett. **91**, 255003 (2003).

[42] G. Gogia and J. C. Burton, Phys. Rev. Lett. **119**, 178004 (2017).

[43] X. G. Wang, A. Bhattacharjee, and S. Hu, Phys. Rev. Lett. **86**, 2569 (2001).

[44] S. Nunomura, J. Goree, S. Hu, X. Wang, A. Bhattacharjee, and K. Avinash, Phys. Rev. Lett. **89**, 035001 (2002).

[45] V. Nosenko and J. Goree, Phys. Rev. Lett. **93**, 155004 (2004).

[46] D. Huang, S. Lu, and Y. Feng, Phys. Rev. E **103**, 013211 (2021).

[47] R. Belousov, E. G. D. Cohen, and L. Rondoni, Phys. Rev. E **96**, 022125 (2017).

[48] J. P. Hansen and I. R. McDonald, *The Theory of Simple Liquids*, 2nd ed. (Elsevier Academic Press, Amsterdam, 1986).

[49] Y. Feng, J. Goree, B. Liu, and E. G. D. Cohen, Phys. Rev. E **84**, 046412 (2011).

[50] J. Ashwin and A. Sen, Phys. Rev. Lett. **114**, 055002 (2015).

[51] L. D. Landau and E. M. Lifshitz, *Fluid Mechanics*, 2nd ed. (Pergamon Press, Oxford, 1987).

[52] R. Lakes, *Viscoelastic Materials*, 1st ed. (Cambridge University Press, Cambridge, UK, 2009).

[53] R. A. Adams and C. Essex, *Calculus: A Complete Course*, 9th ed. (Pearson Press, Ontario, 2018).

[54] P. M. Chaikin and T. C. Lubensky, *Principles of Condensed Matter Physics* (Cambridge University Press, Cambridge, 2000).